A LASER-BASED BOTTOM PROFILER SYSTEM FOR MEASURING NET SEDIMENT TRANSPORT RATES IN AN OSCILLATORY WATER TUNNEL

Jing Yuan[1], Wang Dongxu[2] and Ole S. Madsen[3]

Abstract

Oscillatory Water Tunnel (OWT) is a widely used facility for full-scale experiments of coastal boundary layer flows and sediment transport. In this paper, a Laser-based Bottom Profiler system (LBP) is developed for measuring bedform morphodyanmics and sediment transport in an existing OWT. This system adopts laser-image techniques, so the bottom profile can be easily measured with minimum interference to an on-going test. Validation tests demonstrate that the system can afford measurements with a very high accuracy. Some preliminary tests in the ripple-bed regime are reported to further show the capability of the LBP. Under sinusoidal oscillatory flows, 2-dimensional (2D) ripples can be slowly developed from a flat movable bottom, and both ripple height and length grow with time. The shape of individual ripples is closer to sinusoidal profiles than to parabolic profiles generalized from small-scale flume experiments, especially for strong flow conditions. For the tests on sloping bottoms, it is observed that the 2D ripples migrate downslope with a constant speed, and the speed increases linearly with bottom slope. A net sediment transport rate in the downslope direction is also observed to increase linearly with bottom slope, which is in agreement with similar studies in the sheet-flow regime.

Key words: oscillatory water tunnel, sediment transport, vortex ripples, full-scale experiments, bottom profiler

1. Introduction

Coastal sediment transport is closely related to beach management and stability of coastal structures, and therefore is of primary interest to the coastal-engineering community. Laboratory experiment is a key research avenue for in-depth understanding of this complex phenomenon. Many previous investigations are conducted using Oscillatory Water Tunnels (OWT), which are U-shaped tunnels with a piston located at one end producing oscillatory flows in the horizontal test channel. The key merit of OWT is that full-scale simulations of wave or wave-current boundary layer flows can be easily achieved, so they are widely used for studying coastal boundary layer flows (e.g. Jonsson and Carlsen, 1976, Yuan and Madsen 2015) and coastal sediment transport (e.g. Ribberink and Al-Salem, 1995, O'Donoghue and Wright, 2004).

A Wave-Current-Sediment (WCS) facility, which is an OWT, has been developed at the Hydraulic Engineering Lab of the Civil and Environmental Engineering Department at the National University of Singapore. This facility (as shown in Figure 1) can precisely produce controllable oscillatory flows or wave-current flows. The main part is a 10m-long test section with a 50cm-deep and 40cm-wide rectangular cross section. It has glass sidewalls and acrylic lids along its entire length, which facilitates the deployment of laser- or image-based instruments. A 20cm trough of the test section is designed for holding sediments. Two 1m-diameter stainless steel vertical cylindrical risers are connected to the two ends of the test section through honeycomb flow filters. One riser contains a programmable, hydraulically actuated piston, manufactured by MTS, to generate prescribed oscillatory wave motions in the test channel, and the other is open to the atmosphere. The design limits for excursion, velocity, and acceleration of oscillatory flows in the test section are 2m, 2m/s, and 2m/s^2, respectively, for periods 2s<T<12s. A Boerger EL1550 Rotary Lobe pump is connected to introduce currents of up to 60cm/s average velocity in the test channel. Through a number of preliminary studies (see Yuan and Madsen, 2014, 2015), we have confirmed the OWT's ability to reproduce,

[1]Assistant professor, National University of Singapore, Block E1A #07-03, 2 Engineering Drive 1, Singapore 117576, Ph (65) 65162160
[2]Graduate student, National University of Singapore, Block E1A #07-03, 2 Engineering Drive 1, Singapore 117576
[3]Donald and Martha Harleman Professor Emeritus of Civil and Environmental Engineering, R. M. Parsons Laboratory 48-317, MIT, Cambridge, MA02139, USA. Ph. (1) 617-253-2721

with extreme accuracy, any specified flow conditions.

To further use the WCS for sediment-transport research, it is necessary to establish a methodology for measuring the topography of the moveable sand bed and the net sediment transport rate. To this end, a Laser-based Bottom Profiler (LBP) is developed. Some brief introduction of this system was provided by Yuan and Madsen (2017). In this paper, we further provide some detailed information of the LBP. Some preliminary results of experiments in the ripple-bed regime are also provided to demonstrate the capability of the LBP.
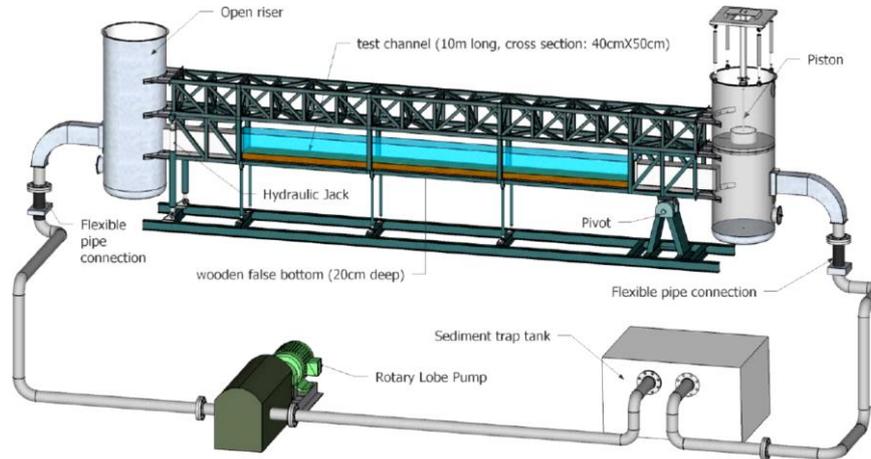
Figure 1 3D sketch of the WCS facility

2. The Laser-based Bottom Profiler (LBP)

The LBP system is designed to measure the bottom profile of the 9-m long moveable bed in the WCS. The general concept of the LBP is in Figure 2. Since the WCS facility has a transparent acrylic lid, laser sheets can be easily introduced into the test channel from the top. Here we use several laser-sheet units to create a continuous laser line on the bottom in the longitudinal direction along the test section (indicated by the thick red solid line). A few digital cameras capture images of the laser line in a dark environment through the sidewall viewing windows, so the obtained images show red laser lines representing the movable bed in a black background, as indicated in Figure 2b. A bottom profile can therefore be quantitatively determined by tracing the peak local redness value along the laser line. For estimating net sediment transport rate, the change of bottom profile can be quantified by comparing images before and after one experiment (see Figure 2b). This concept requires that the sand bottom remains 2-dimensional, which can be satisfied in many experiments, e.g. sheet-flow conditions.
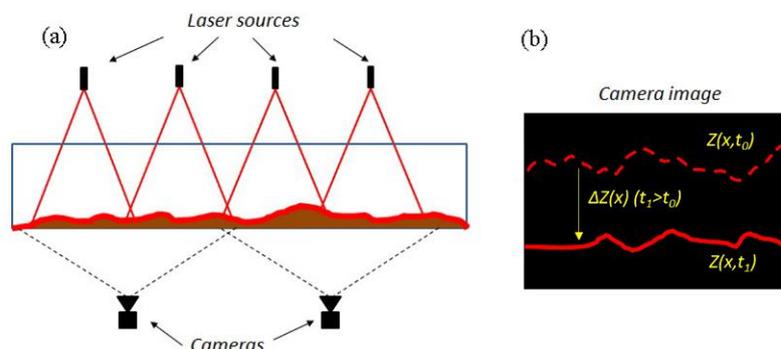
Figure 2 the general concept of the LBP system: (a) system setup, (b) image of laser line on the moveable bed

2.1. *System components*

The main components of the LBP system include the laser units and the cameras. Since some 3-

dimensionality is inevitable, we produce two laser lines located symmetrically on both sides of the lateral centerline of the WCS with half-width distance (20 cm) apart. Therefore, two measurements following the two laser lines can be obtained, and their average is taken as the final measurement. Each laser line is produced with 12 laser units carefully mounted within the overlying thrust of the WCS (as shown in Figure 3). One laser unit covers a 75cm segment, and some overlap (about 3-5cm) is produced between nearby units to avoid gaps due to an uneven bottom. Nikon D5200 cameras (resolution 6000×4000) are used to capture images of the laser lines. These cameras are equipped with remote-triggering controllers, direct power supply, and images can be wirelessly downloaded to mobile devices, so we do not need to touch the camera body after installation, preventing unwanted disturbance. The entire test channel is covered by six cameras with each camera covering a 1.5m horizontal span. The overlapped region will be trimmed off when combining measurements. As shown in Figure 3, the cameras are carefully positioned on a Camera Support Beam (CSB) with a 1.5m spacing, which can be tiled in unison with the test section, so we can also use the LBP for experiments with a sloping WCS. Some permanent markers are drawn on the test sections' sidewall in front of the cameras, which are used for fine-adjusting the camera orientation and obtaining calibration parameters.
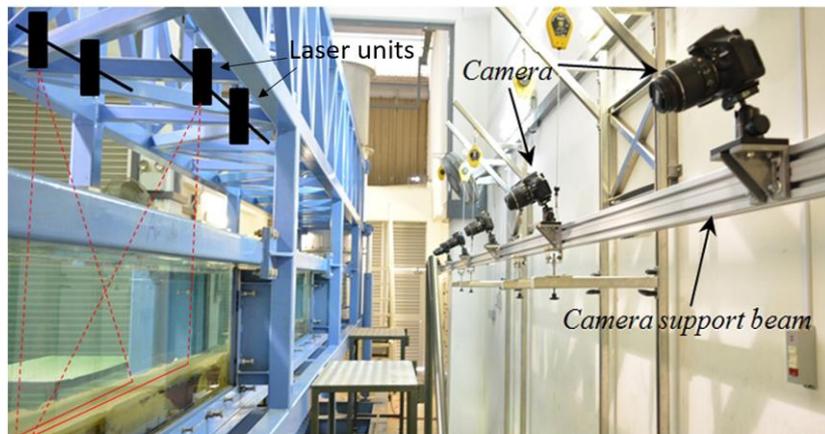
Figure 3 Setup of the LBP

2.2. *Image processing*

The raw camera image suffers some perspective distortion, so a calibration image showing the markers on the sidewalls is first captured for image rectifications. As shown Figure 4a, the camera's perspective distortion makes vertical lines near the edges of the image become tilted, which must be rectified before image analysis. Using the image correction function of Adobe Photoshop CS6, we can nicely remove this distortion (see Figure 4b). Since there will be no change in camera settings when subsequently capturing the laser-line images in a dark background, the same rectification can be applied. Thus, the image rectification performed to the calibration image is recorded in Adobe Photoshop CS6 and automatically applied to the following laser-line images.

As shown in Figure 5a, the redness decays towards edges of the laser-line's image. Thus, we assume that the digital redness value (from 0 to 255 with 0 being black and 255 being red) across the image of each laser line follows a normal distribution:

$$B(X,Z) = \frac{1}{\sigma(X)\sqrt{2\pi}} e^{-\frac{(Z-Z_b(X))^2}{2\sigma(X)^2}} \tag{1}$$

where B is the image redness (0 to 255), (X, Z) are the horizontal and vertical image coordinates (in pixels) with the origin set at the lower-left corner of the image, respectively, $\sigma(X)$ is the standard deviation of the normal distribution and $Z_b(X)$ is the vertical coordinate of the distribution's peak (in pixels), which is taken as the location of the movable bed. An example of such a fitting to actual measurements is given in Figure

5b. Since the maximum redness is capped at 255, the data points with redness value being 255 are not included in the fitting. The rest of the data points indeed agree nicely with the fitted curve, indicating that the choice of a normal distribution is reasonable. The normal-distribution fitting can be performed at every horizontal location X to get a bottom profile $Z_b(X)$ for each camera. To further combined measurements from the six cameras to a universal longitudinal profile, some pre-determined calibration parameters are required.
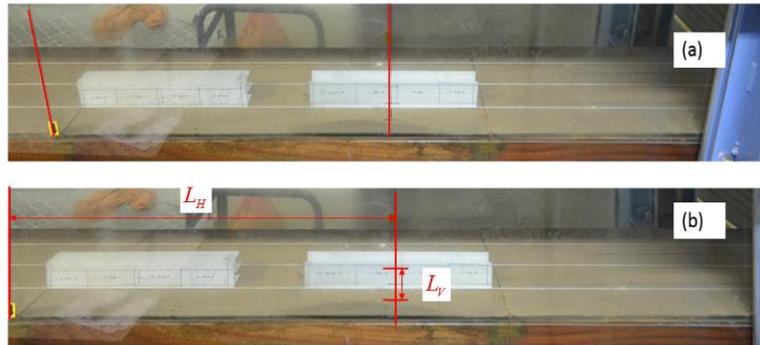
Figure 4 Image rectification based on the calibration image: (a) raw image, (b) rectified image
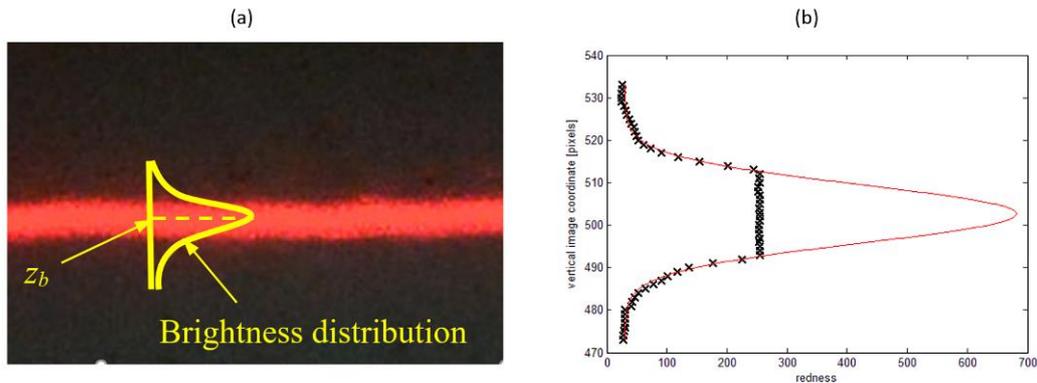
Figure 5 Locating the movable bottom on the laser-line image (a) laser-line image (b) fitted normal distribution (crosses are measured redness values, solid line is the fitting)

2.3. *Calibration*

Calibration parameters in both horizontal and vertical directions are required to translate the results from image processing. Since camera settings may slightly change in different tests, calibration must be done before each test. The general idea for calibration is as follows. Based on some target markers on the front sidewall of the WCS, we first obtain the horizontal and vertical calibration parameters for the vertical plane of the WCS' front sidewall. We then translate them into those for the vertical planes of the two laser lines using pre-calibrated empirical formulas.

The calibrations at the sidewall are obtained using the calibration image, as shown in Figure 4. For each camera, some permanent markers are drawn on the sidewall facing the cameras, including two long vertical lines (with a distance of L_v apart) and two short horizontal lines (with a distance of L_h apart). By reading the number of pixels, N_h, between the two vertical marking lines on the rectified calibration image (Figure 4b), a horizontal calibration parameter, $c_{h,f}$, can be obtained as $c_{h,f}=L_h /N_h$. Similarly, the vertical calibration parameter, $c_{v,f}$, can be obtained as $c_{v,f}=L_v /N_v$, where N_v is the number of pixels between the two short horizontal marking lines. The empirical formulas are established based on a large dataset obtained as follows. We placed calibration objects with markers at the vertical plane of the laser line, so a calibration image will contain these objects, e.g. the aluminum bars in Figure 4. Using the same method for obtaining $(c_{h,f}, c_{v,f})$ for the front sidewall, we can determine the calibrations, (c_h, c_v), at the laser-line's vertical plane. The two pairs of calibration parameters, i.e. $(c_{h,f}, c_{v,f})$ and (c_h, c_v), obtained from the same calibration image, are apparently correlated. By slightly adjusting the cameras, a large set of calibration images with slightly different values

of calibration parameters can obtained, so a large dataset of ($c_{h,f}$, $c_{v,f}$, c_h, c_v) can be established for calibrating empirical formulas. Here we propose to correlate c_h with $c_{h,f}$ and c_v with $c_{v,f}$. Figure 6 shows c_v versus $c_{v,f}$ for the laser line closer to the camera. The data includes measurements from the six cameras. Apparently, there is a linear relationship between the two, which is also true for the horizontal calibration and the other laser line. Thus, we can fit the following linear function to the data

$$c_{v,i} = a_{v,i} \cdot c_{v,f} + b_{v,i}$$
$$c_{h,i} = a_{h,i} \cdot c_{h,f} + b_{h,i}$$

(2)

where i=1,2 for two laser lines, and ($a_{v,i}$, $b_{v,i}$, $a_{h,i}$, $b_{h,i}$) are parameters obtained from data fitting. The discrepancy between the prediction using the fitted formula and the actual measurements are of the order 0.1%, so this methodology can afford a very accurate determination of the calibration parameters.
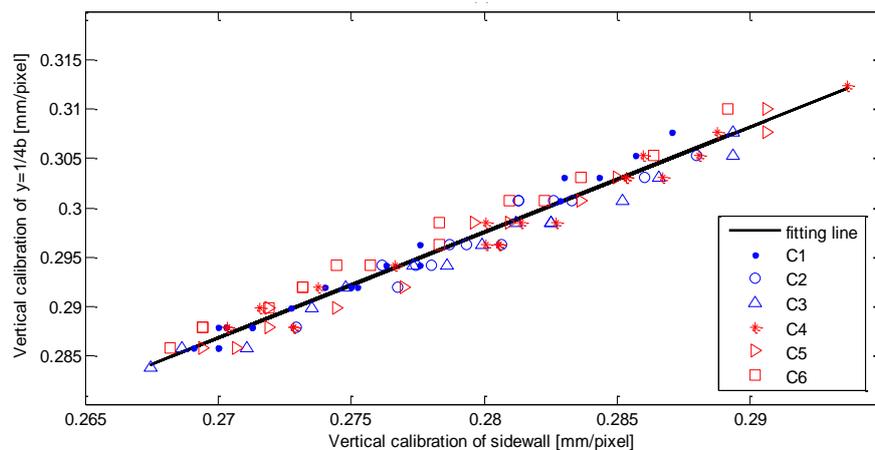
Figure 6 Empirical formula for correlating the vertical calibration parameter of a laser line (the one closer to the camera) with that of the front sidewall (C1 to C6 indicates six cameras)

3. Measuring bottom profile with the Laser-based Bottom Profiler (LBP)

With the image-processing method introduced in section 2.2, the coordinate of the laser line, $Z_b(X)$, can be obtained, where Z_b and X (both in pixels) are the vertical and horizontal coordinates with the origin at the lower-left corner of the image. It should be noted that the origins of the six cameras are not necessarily at the same physical vertical level, so to further convert and combine $Z_b(X)$ into a bottom profile, we need to establish a common datum Z=0 across the six cameras for adjusting the vertical coordinates. This is achieved by constructing a longitudinal reference line on each image, which works as Z=0, as follows.

The reference line must be in the same vertical plane aligned with the vertical laser sheet that produces the bottom laser line. It also must be a physically straight line parallel to the longitudinal direction of the test section, and therefore should appear curved on the images due to camera distortion. Since we do not want to introduce any physical object inside the test section, the reference line must be conceptually determined. For each camera, we draw three pairs of markers on the two sidewalls of the test channels, e.g. A1-A2, B1-B2 and C1-C2 in Figure 7a. All the markers are located at the same level distance below the lids, and each pair of markers are at the same longitudinal location of the test section. Thus, a straight line connecting a pair of markers, e.g. line A1-A2 in Figure 7b, will have one intersecting points with the vertical plane of the laser line. A number of such intersecting points can define a physically straight line that satisfies the requirement for the reference line. We choose to have three intersecting points, e.g. points *a*, *b* and *c* in Figure 7b, determined for the three pairs of markers, so we can fit a parabolic curve, $Z_R(X)$, to the points, e.g. the dashed line in Figure 7b, which can be taken as the reference line. Having three-points and a parabolic curve allows the obtained reference line to be slightly curved, mimicking camera distortion. When we pin-down the pairs of markers for all six cameras, we made the test section horizontal, and filled water to a desired level (about 30cm above the sand bed). We carefully drew the markers on the sidewalls at the level of the free water surface, so all markers are with the same distance from the lid. In such a way, the obtained reference lines

will represent a common datum of $Z=0$ for all the six cameras, as they are with the same physical distance below the lids. This allows us to directly combine the obtained bottom profiles from individual images after adjusting vertical coordinates.

The intersecting points, e.g. point b in Figure 7b, is located as follows. Since the horizontal calibration parameter c_h can be pre-determined, and the horizontal distance from a pair of markers to the vertical marking line representing the middle of the camera's coverage, can be pre-measured, e.g. λ_{BC}, so the X-coordinate of the intersection can be calculated, e.g. the X-coordinate of point b is:

$$X_b = X_C - \frac{\lambda_{BC}}{c_h} \tag{3}$$

where X_C is the X-coordinate of the vertical marking line. The Z-coordinate of the intersecting point can subsequently be determined using the fact that this point is on the straight line connecting the two corresponding markers, of which the image coordinates can be directly read from the image.

With the reference line, which serves as the $Z=0$ datum, and the pre-determined vertical calibration parameter, a bottom profile is obtained as:

$$z_b(X) = c_v \cdot [Z_b(X) - Z_R(X)] \tag{4}$$

The physical horizontal coordinate, x, is determined through

$$x = c_h \left(X - X_{C,i} \right) + x_{c,i} \tag{5}$$

where c_h is the horizontal calibration parameter, $X_{C,i}$ is the image X-coordinate (in pixels) of the vertical marking line representing the center of the i-th camera's coverage, and $x_{c,i}$ is the physical longitudinal coordinate of i-th camera, which takes the value

$$x_{c,i} = 0.75m + (i-1) \cdot 1.5m, \ 1 \le i \le 6 \tag{6}$$

For each camera, the measurements outside its intended coverage, i.e. more than 0.75m from $x_{c,i}$, are removed, and the measurements from the six cameras can be directly combined to give a universal bottom profile.
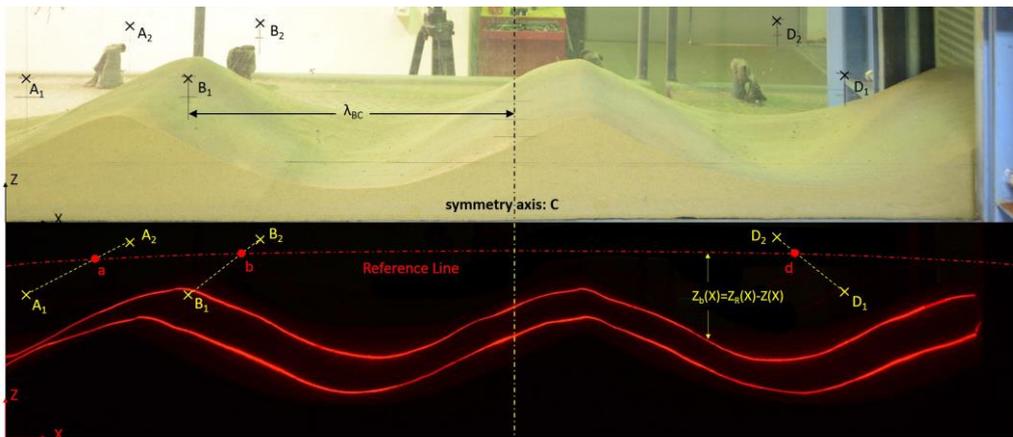
Figure 7 Determination of the reference line for calculating bottom profile

For determining net sediment transport rate, only the change of bottom profile, $\Delta z_b(x)$, is required, so there is no need to construct such a reference line. By comparing the image coordinates of the laser line before and after a test, a change of bottom profile, $\Delta Z(X)$ in pixels can be direct obtained, as shown in Figure 2b. Using the calibration parameters, ΔZ can be simply translated into Δz_b, i.e. $\Delta z_b = c_v \Delta Z$, while the horizontal coordinate is determines following equations (5) and (6).

To demonstrate the accuracy of the LBP system in measuring bottom profile, two preliminary tests were conducted. In the first test, circular arcs cut from PVC pipes were glued onto a flat substrate to form a wavy

surface, of which the bottom topography can be easily determined. The arcs are about 15-17mm in height and 65-70mm in length, so they resemble small vortex ripples. The LBP system is used to measure the bottom profile of this wavy surface. As presented in Figure 8, the measurements (black dots) closely follow the actual bottom profiles (colored curve). The discrepancies are generally less than 0.1mm, suggesting that the system can very accurately measure the bottom profile. In the other preliminary test, we took two images of an untouched sand bottom (sediment diameter d_{50}=0.24mm). The difference of two bottom profiles Δz_b should be zero, so any non-zero Δz_b therefore indicates the system error of the LBP. The obtained Δz_b is essentially a random noise with a standard deviation of O(0.1 mm) and a zero mean value. This suggests that the LBP is able to measure bottom profile (or change) with a 0.1 mm inaccuracy, which is comparable to the diameter of fine sands.
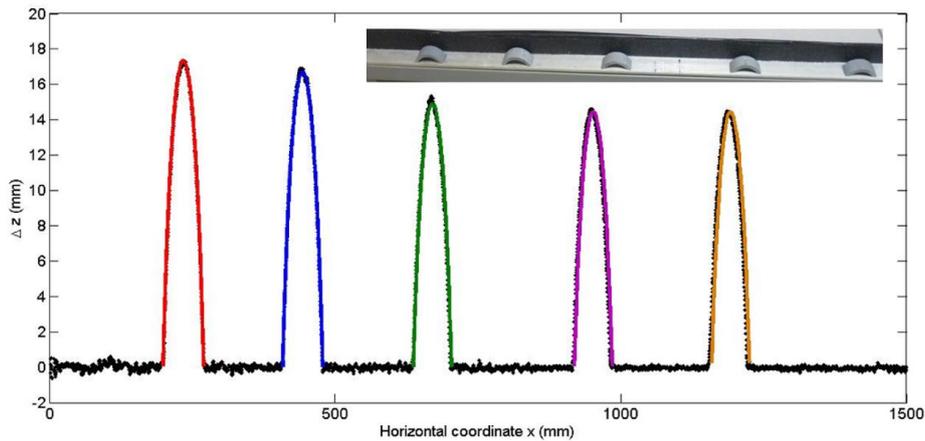
Figure 8 A preliminary test for the accuracy of the LBP system

4. A case study

The LBP system was used by Yuan et al. (2017) for measuring the net bottom-slope-induced sediment transport rate under sinusoidal oscillatory flows in the sheet-flow regime. In their work, the net transport rate was estimated based on the principle of sand volume conservation and the LBP measurements of bottom profile change, Δz_b. Their experimental results suggest that the accuracy of the measured net transport rate is of the order 10^{-6} m²/s, which is equivalent to a mass transport rate of the order a mere 10 kg/hour/m. For tests in the sheet-flow regime the obtained net sediment transport rate is always in the downslope direction, and depends linearly on bottom slope. The reader is referred to their paper for more details. In this paper, we present some preliminary results of a similar study in the ripple-bed regime, which further demonstrates the capability of the LBP system. All tests are conducted with coarse sands (d_{50}=0.51mm) and sinusoidal oscillatory flows. The flow conditions and bottom slope of the WCS for the tests included in this paper are presented in Table 1. Measurements of net transport rate are reported for two tests (TB01 and TB02) on sloping bottoms, while the rest four tests only have measurements of ripple geometry.

Table 1 Experimental conditions and some key measurements (U_{bm} and T are the amplitude and the period of the free-stream sinusoidal oscillatory flow, β is bottom slope of the WCS, η and λ are the height and the length of the equilibrium ripples, respectively, and q_{net} is net sediment transport rate).

Test ID	U_{bm} [m/s]	T [s]	β [°]	η [mm]	λ [mm]	q_{net} [10^{-6} m²/s]
TA01	0.30	6.25	0.0	77	396	-
TA02	0.40	6.25	0.0	92	456	-
TA03	0.80	6.25	0.0	127	689	-
TB01	0.75	4.17	1.6	82	531	-16
TB02	0.75	4.17	2.6	82	541	-24
TC	0.40	3.13	0.0	40	262	-

4.1. *Development of vortex ripples under oscillatory flows*

All tests, except TB01 and TB02, start with a flat sand bed, so the history of ripple development under oscillatory flows can be easily documented using the LBP system. Based on laser images (see Figure 9), three typical stages of ripple development can be identified. Ripple marks, which are small in both length and height, first appear on the initially flat bottom within $O(10)$ periods, and the occurrence time is longer for weaker flow conditions. These ripple marks are reasonably uniform and 2-dimensional. Since they are very small in size, there is not much flow separation at their crests, and consequently no significant sediment suspension is observed. LBP system can be straightforwardly applied to measure the bottom profile without stopping the test. Through Fourier analyzing the measured bottom profile, a root-mean-square ripple height and an average ripple length can be estimated. Figure 9(a,b) shows the development of these two quantities for test TC (U_{bm}=0.4m/s, T=3.125s) during the initial 120 periods. Apparently both ripple height and ripple length increase with time. This suggests that the assumption of an invariant ripple length in some linear instability analysis may be questionable. As the ripple marks grow in size, flow separation around their crests become strong enough to suspend a large quantity of sands, and the bottom profile becomes increasingly 3-dimensional and irregular. This usually occurs after $O(100)$ periods, and lasts for a long time. During this process, the LBP system must be applied with temporarily stopping the on-going test, as the suspended sands make the image very blur, but the interference is minimum as the bedform development is very slow. In most of our tests, 2-dimensional and uniform ripples will eventually appear after hundreds or thousands of wave periods (equivalent to a few hours), as shown in the laser image at the lower-right corner of Figure 9. In some tests, we found that this long process can be greatly expedited by slightly tilting the WCS. For instance, when test TC was conducted over a horizontal bed, we did not obtain 2D equilibrium ripples after running 8 hours of experiments (~9000 periods). However, after continuing the test on a 2.6° slope, 2D equilibrium ripples quickly appear after a few hundreds of wave period. Our hypothesis is that the bottom slope produces a net sediment transport rate, which facilitates the re-distribution of sands for ripple development.
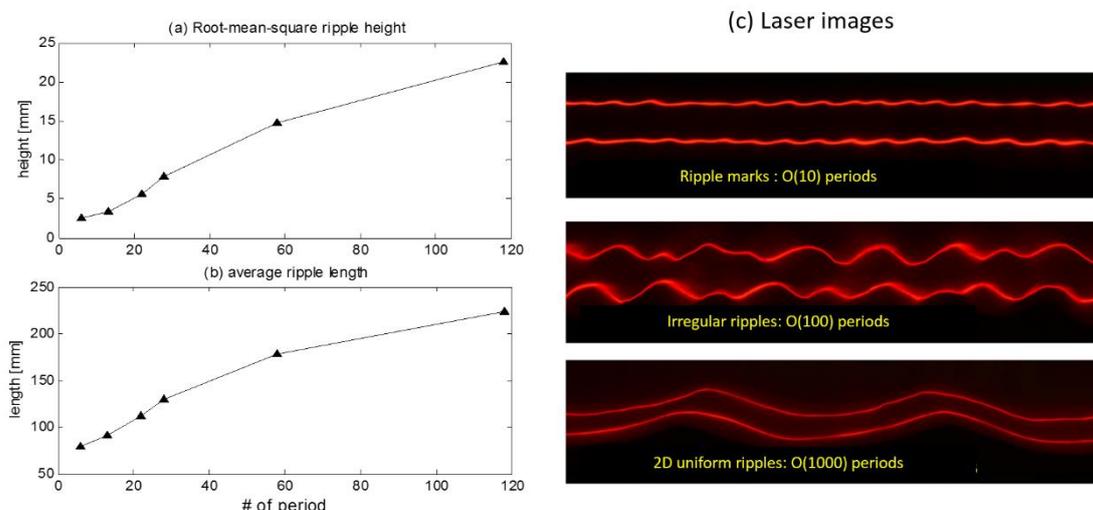
Figure 9 history of ripple development from a flat sand bottom: (a) variation of root-mean-square ripple height for test TC, (b) variation of average ripple length for test TC, (c) typical laser images showing the change of bottom profile.

4.2. *2-dimensional uniform ripples*

For most flow conditions, a train of 2-dimensional uniform ripples eventually cover the major part of the test section after hundreds or thousands of wave periods. We subsequently ensemble-average them into an average ripple profile, which is used to determine the ripple height (the vertical distance from the crest to the trough) and the ripple length (the horizontal distance between two troughs). The results for selected tests are presented in Table 1. Generally speaking, the ripple length increase with the excursion amplitude, $A_{bm}=U_{bm}T/2\pi$, of the oscillatory flow. The ripple steepness, η/λ, is consistently within 0.15-0.2. These results are in good agreement with those from similar studies. More in-depth discussions of ripple dimensions will

be provided in a future journal paper.

The highly-accurate LBP measurements allow us to further investigate the shape of the 2D uniform ripples, which is closely related to the sediment transport processes. A key finding is that the ripple shape is not self-similar. Figure 10 presents the average ripple profiles for two typical cases, TA01 and TA03. The flow condition under TA01 (U_{bm} =0.3m/s and T=6.25 period) just slightly exceed the critical condition for incipient motion, so not much sediment suspension occurs. TA03 (U_{bm} =0.8m/s and T=6.25 period) has a much stronger flow conditions, so the suspended sediment clouds can reach 2-3 times the ripple height above the ripple crests (based on visual observations). Figure 10 (a,c) present the average ripple profiles. The gray zone, which indicates the standard deviation from ensemble-averaging individual ripples, is very narrow, suggesting a good periodicity of the ripples. The ripple crests appear quite rounded, which is partly because that ensemble-averaging will smooth the ripple profile. Nevertheless, we can still see that TA01 has a shaper crest than TA03, which can also be observed from the laser images (Figure 10 e,f). It is hypothesized that a sharp ripple crest cannot be maintained under a very strong flow condition. We further fit a Fourier series to the average ripple profiles. As shown in Figure 10b, TA01's profile can be well approximated by the leading two harmonics of its Fourier series, and the second harmonic is about 15% of the first harmonic in amplitude. However, for TA01 (Figure 10d), just the leading first harmonic can very nicely approximate the ripple profile. This suggests that under sufficiently strong flow conditions, the 2D uniform ripples are very sinusoidal, which is against a parabolic shape generalized from small-scale wave flume experiments.
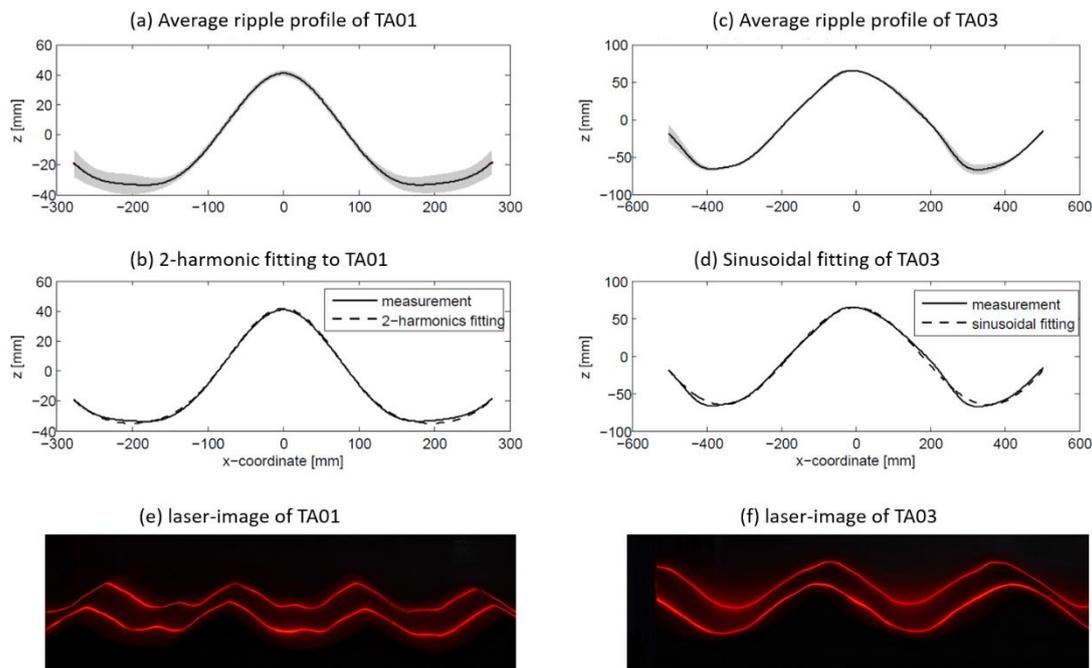
Figure 10 the representative profile of 2D uniform ripples

4.3. *Bottom-slope-induced net sediment transport rate over vortex ripples*

After the 2D uniform ripples are produced on a horizontal bed, the test section of the WCS is tilted to simulate a sloping bottom, and a number of tests are conducted to study the behavior of these 2D ripples and the associated net sediment transport rate. Since the flow is still sinusoidal, the obtained net transport rate is sorely due to the bottom-slope effect. Under most flow conditions, the shape of the 2D ripples changes very slightly as the bottom slope increases from 0 to 2.6°. For instance, the ripple length of TB02 is slightly longer than that of TB01, i.e. 541mm vs 531mm. A key observation is that ripples migrate in the downslope direction with a uniform migration speed. This can be clearly seen from the snapshots of test TB02 presented in Figure 11. The time interval between two snapshots is 190 wave period (or about 13 minutes). The ripple crest moves in the downslope direction with an almost constant displacement between two snapshots, indicating a fairly uniform migration speed. Also, no significant difference in ripple geometry can be observed among

these three snapshots, so ripples migrate with permanent form. By correlating the bottom profile before and after one experiment, the migrated distance and consequently the migration speed can be estimated. For TB01 and TB02, the migration speeds are 2.7mm/s and 4.4mm/s. The results are plotted against the bottom slope in Figure 12a. It can be clearly seen that the migration speed increases almost linearly with the bottom slope.
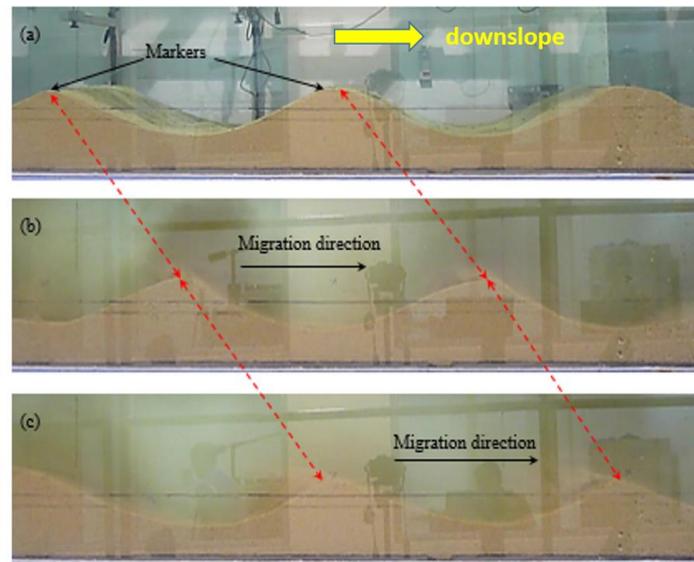
Figure 11 Ripple migration on sloping bottom (test TB02, U_{bm}=0.75m/s, T=6.25s, η=82mm, λ=541mm, slope β=2.6°). The time interval between two successive frames is 190 wave periods.

Following Yuan et al. (2017) the net sediment transport rate along the test section of the WCS is estimated based on the principle of sand-volume conservation and the LBP-measured bottom profile change, i.e.

$$q_s(x) = -\frac{1-\varepsilon}{\Delta T}\int_{x_0}^{x}\Delta z_b dx - \frac{V_0}{\Delta Tb} \tag{7}$$

where ϵ=0.482 is the porosity of the sand bed, ΔT is the test duration, x_0 is the x-coordinate of the downslope end of the test section, V_0 is the volume of sand collected outside $x=x_0$, b is the channel width. A correction proposed by Yuan et al. (2017) is applied for sand-bed compaction. Figure 13 shows a typical example (test TB02) of the obtained net transport rate. Around the middle of the test section, the obtained $q_s(x)$ exhibits some periodic undulations. This is due to the fact that the net transport rate is not uniform across one ripple profile. Thus, we identity a region around the center of the WCS, of which the width is a few ripple lengths, so the average $q_s(x)$ within this region is the ripple-averaged net transport rate, q_{net}. The obtained q_{net} is always in the downslope direction. This is not surprising, as it is always easy to move sediments in the downslope direction. The results of the two tests, TB01 and TB02, are plotted against bottom slope in Figure 12b. As we can see, there is a fairly good linear relationship between net transport rate and bottom slope, despite that we only have two points. This is in agreement with the results from similar sheet-flow tests. Further discussions on these experimental results will be provided in a future journal publication.

5. Conclusions

In this study, a laser-based bottom profiler system is developed for an existing oscillatory water tunnel, which can measure bottom profile and net sediment transport rate with an accuracy of O(0.1mm) and O(10^{-6}m^2/s), respectively. To demonstrate the capability of this system, some preliminary results of tests in the ripple-bed regime are reported. Periodic and amazingly uniform 2D vortex ripples are developed from an initially flat bottom after O(100~1000) wave periods, and they migrate downslope at a constant speed on sloping bottoms. The shape of equilibrium vortex ripple changes from sharp-crested to nearly sinusoidal, as the flow condition increases. The bottom-slope-induced net sediment transport rate under purely sinusoidal oscillatory flows

varies linearly with (mild) bottom slope, for both sheet-flow and rippled-bed regimes.
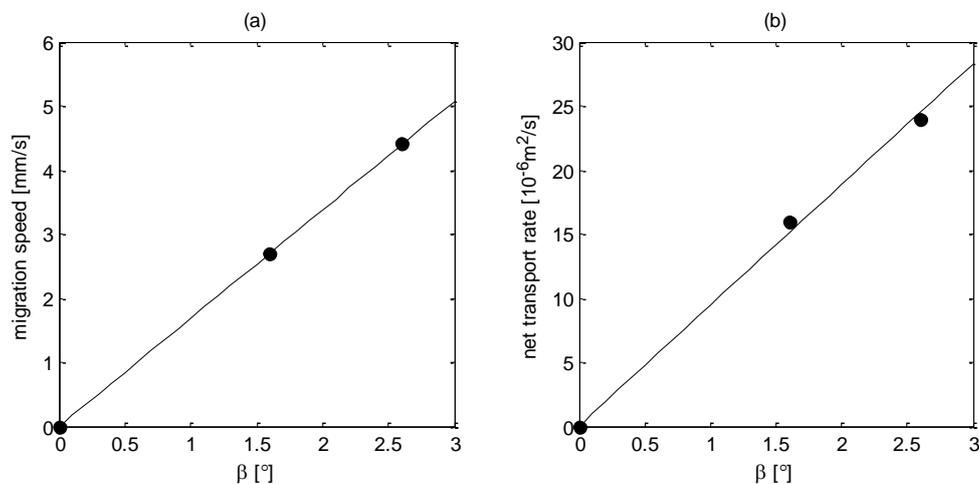
Figure 12 Migration speed and net sediment transport rate for test TB01 and TB02.
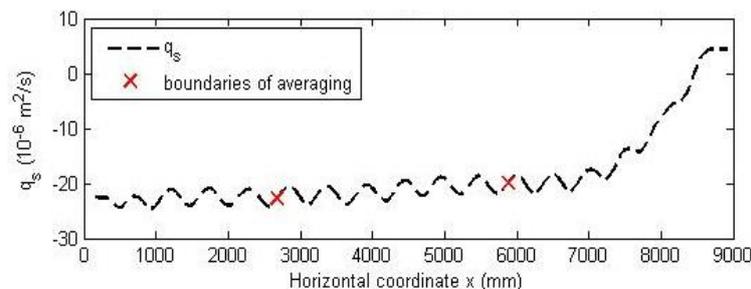
Figure 13 net sediment transport rate for test TB02

Acknowledgements

References

Jonsson, I. G., & Carlsen, N. A. (1976). Experimental and theoretical investigations in an oscillatory turbulent boundary layer. Journal of Hydraulic Research, 14(1), 45-60. doi:10.1080/00221687609499687

O'Donoghue, T., & Wright, S. (2004). Flow tunnel measurements of velocities and sand flux in oscillatory sheet flow for well-sorted and graded sands. Coastal Engineering, 51(11–12), 1163-1184. doi:10.1016/j.coastaleng.2004.08.001

Pedocchi, F., & García, M. H. (2009). Ripple morphology under oscillatory flow: 1. Prediction. Journal of Geophysical Research: Oceans, 114(C12), C12014. doi:10.1029/2009JC005354

Ribberink, J. S., & Al-Salem, A. A. (1995). Sheet flow and suspension of sand in oscillatory boundary layers. Coastal Engineering, 25(3-4), 205-225. doi:10.1016/0378-3839(95)00003-t

Yuan, J., Li, Z., & Madsen, O. S. (2017). Bottom-slope-induced net sheet-flow sediment transport rate under sinusoidal oscillatory flows. Journal of Geophysical Research: Oceans, 122(1), 236-263. doi:10.1002/2016JC011996

Yuan, J., & Madsen, O. S. (2014). Experimental study of turbulent oscillatory boundary layers in an oscillating water tunnel. Coastal Engineering, 89, 63-84. doi:http://dx.doi.org/10.1016/j.coastaleng.2014.03.007

Yuan, J., & Madsen, O. S. (2015). Experimental and theoretical study of wave–current turbulent boundary layers. Journal of Fluid Mechanics, 765, 480-523. doi:doi:10.1017/jfm.2014.746